



Contents lists available at ScienceDirect

International Journal of Solids and Structures

journal homepage: www.elsevier.com/locate/ijsolstr



Reconfigurable surfaces employing linear-rotational and bistable-translational (LRBT) joints



Yang Li ^{a,b,*}, Anjini Chandra ^c, Charles J. Dorn ^b, Robert J. Lang ^d

^a The Institute of Technological Sciences, Wuhan University, Wuhan 430072, PR China

^b Graduate Aerospace Laboratories, California Institute of Technology, 1200 E. California Blvd, Pasadena, CA 91125, United States

^c California Institute of Technology, 1200 E. California Blvd, Pasadena, CA 91125, United States

^d Lang Origami, Altadena, CA 91001, United States

ARTICLE INFO

Article history:

Received 19 June 2020

Received in revised form 15 September

2020

Accepted 22 September 2020

Available online 6 October 2020

Keywords:

Reconfigurable structures

Isometric transformation

Origami

Torsional hinges

Metric-changing transformation

Bistability

Compliant mechanisms

ABSTRACT

Reconfigurable surfaces are useful in many applications. This paper proposes a type of reconfigurable surfaces that consist of rigid elements (tiles) connected by novel compliant joints. Depending on the actuation, these novel connecting joints can either operate as torsional hinges, which create isometric transformation (like origami folding) between connected tiles, or bistable translational springs, which accommodate metric-changing transformation between connected tiles. A specific example of a reconfigurable surface with square tile shape that can morph into flat, cylindrical (in two different directions), and spherical configurations with simple actuation is given.

© 2020 Elsevier Ltd. All rights reserved.

1. Introduction

Reconfigurable surfaces are useful for applications that require several service configurations, which can lead to more powerful and compound devices. The application that this paper corresponds to is for an antenna that has a mechanically reconfigurable platform. Such platforms can help the antennas to adjust polarization (Yao and Georgakopoulos, 2018), frequency of active antennas (Wu, 2019; Chaudhari, 2018; Lee, 2019; Khan, 2019) and of passive ones (Fuchi, 2012, 2017; Abadi et al., 2016), and their radiation pattern (Russell et al., 2019; Liu et al., 2017; Georgakopoulos, 2019; Shah and Lim, 2019; Carrara, 2019) through active mechanical reconfiguration. A mechanically reconfigurable platform can also make the antenna deployable so that it is easier to be transported (Seiler, 2018; Zhu and Feng, 2019; Sessions, 2018; Costantine, 2016; Shah et al., 2019).

This paper aims at providing a mechanically reconfigurable platform for a novel antenna array concept introduced in (Williams et al., 2020), in which it breaks the trade-off between

steering range, i.e., field of view, and directivity, i.e., fidelity in a specified direction. Traditionally, a phased array antenna with a flat configuration has high fidelity in the normal direction but a rather narrow field of view, and a conformal antenna on a curved surface can have a large field of view but relatively low fidelity (Guy, 1999). This is due to the well-known property that directivity is proportional to cross-sectional areas for large arrays (Kildal et al., 2017; Gustafsson and Capek, 2019). A novel concept to combine the merits of the two through mounting antenna tiles on a mechanically reconfigurable platform was proposed in (Williams et al., 2020).

Specifically, the platform needs to morph in between flat (the highest fidelity in the normal direction while the narrowest field of view), cylindrical 1 and 2 (a wider field of view in two different directions while correspondingly lower fidelity), and spherical (the widest field of view in all directions and the lowest fidelity) configurations, as shown in Fig. 1 where the spherical configuration is unknown and is proposed in this paper. As a result, the field of view and the directional fidelity of the antenna can be tuned during service through mechanical reconfiguration. Fig. 1(a)–(c) involve isometric transformation, i.e., the distances (following the surface) between nodes are not changing, and Fig. 1(d) involves metric-changing transformation, i.e., extensions of distances

* Corresponding author at: The Institute of Technological Sciences, Wuhan University, Wuhan 430072, PR China.

E-mail address: yang.li@whu.edu.cn (Y. Li).

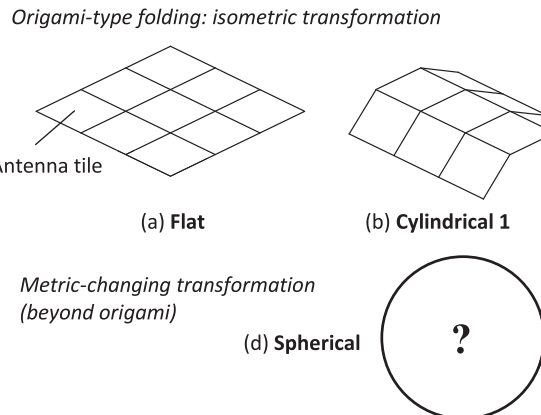


Fig. 1. Four target morphing configurations to be achieved by the mechanically reconfigurable surface.

(following the surface) between nodes are needed. This paper proposes the design method for the reconfigurable surface that satisfies the requirement shown in Fig. 1 while achieving easy manufacturability, simple actuation, and high stiffness. The detailed antenna concept and properties will be reported separately in (Williams et al., 2020).

Active origami can be used to generate reconfigurable surfaces. Most existing work is limited to isometric morphing (Hawkes, 2010; Paik et al., 2011; Peraza-Hernandez et al., 2013), where only folding deformation is involved. Furthermore, these patterns are typically one degree-of-freedom (DOF) origami patterns, such as Miura-ori (Gattas et al., 2013), which are most popular due to their simplicity to control. More sophisticated origami patterns like the waterbomb base (Chen, 2016) and Resch's pattern (Tachi, 2013) can provide metric-changing morphing if only tracking the overall shape (only considering certain tiles). For instance, these origami patterns can morph from flat to spherical configurations. However, complex fold patterns introduce prohibitive manufacturing challenges and lead to high DOF structures requiring complex actuation (Li, 2020; Magliozzi, 2017). Another similar technique is to use kirigami and extensible elements to achieve metric-changing transformation and reconfigure a flat plane to a 3D surface (Choi et al., 2019; Chiang et al., 2018; Chen et al., 2017), but the tile or nodal arrangement cannot be aligned as shown in Fig. 1 and provide the required isometric deformation.

Alternatively, active elastomers can produce both isometric and metric-changing deformation. Through manipulation of the magnetic (Kim, 2018), electrical (Hajiesmaili and Clarke, 2019), heat (Plucinsky, 2018; Guseinov, 2020), or humidity (Ma, 2013) field, active elastomers can produce differential swelling in different directions and correspondingly generate designed overall deformation. However, compared to active origami, active elastomers generate relatively small curvature change with slow actuation response, and their low stiffness is problematic for maintaining shape in operation as a morphing platform.

Another method is to discretize the surface and control each part individually (Page et al., 2005; Leithinger, 2011), which can provide the most flexible reconfiguration comparing to active origami and active elastomers. However, this method is heavy, expensive, and unnecessary for applications that require only certain specified reconfigurations (such as those described in Fig. 1).

The solution proposed in this paper is to design the connection between square tiles that can work as (1) a torsional hinge to provide isometric transformation (origami-like folding) and (2) a bistable translational spring to accommodate metric-changing transformation that can only be initiated when the energy barrier

(due to the bistability) is overcome. Global bi/multistability can simplify the actuation (Li et al., 2019) during metric-changing transformation. From the literature, lamina emergent torsional (LET) joints (Jacobsen, 2009; Wilding et al., 2012) can produce integrated torsional hinges, and snap-through slender beams (Chiang et al., 2018; Qiu et al., 2001; Zhao, 2008) can provide bistable translational springs. This paper proposes the integration of the two, which will be referred to as linear-rotational and bistable-translational (LRBT) joints. In consequence, it is possible to build an isometric and metric-changing reconfigurable surface that has easy manufacturability (by simply cutting a plate), is easy to actuate (due to the bistability), and is sufficiently stiff (due to the bistability) to maintain shape.

This method can be generalized for other tile shapes and target morphing configurations, which leads to wider applications. Multiple cameras can be mounted on different tiles of a reconfigurable platform to change the overall field of view and resolution. Manufacturing 3D structures from 2D material is useful for optical sensors (Zhang, 2017; Ko, 2008), electronics (Huang, 2019), and so on (Callens and Zadpoor, 2018), to which the LRBT joints might be applicable. Besides morphing surfaces/platforms, LRBT joints might be used for multifunctional origami robots (Rus and Tolley, 2018; Zhakypov and Paik, 2018) where smooth motion is provided by isometric transformation while bistable metric-changing transformation can be used to provide the reconfigurable for different functions or directional propulsion (Chen, 2018).

This paper is laid out as follows. Section 2 presents a deterministic procedure for arranging square tiles on a sphere to form the spherical configuration. Section 3 introduces the design of linear-rotational and bistable-translational (LRBT) joints. As an example, Section 4 provides the design, manufacturing, and actuation of reconfigurable surfaces employing the square tessellation on a sphere and LRBT joints. Section 5 concludes the paper.

2. Arrangement of squares on a sphere

Since a plane, cylinder 1, and cylinder 2 (Fig. 1(a)–(c)) are all developable surfaces, they can all be realized by simple folding (or not folding) of an initially planar shape. Achieving a spherical configuration from an initially planar arrangement of square tiles is more challenging, though. Because a sphere has nonzero Gaussian curvature, the deformation from the plane to the sphere must be non-isometric, or, in simpler terms, the spacing between adjacent tile pairs must vary from tile to tile, as illustrated in Fig. 2.

We assume a sphere of radius R and use unit square tiles. Define

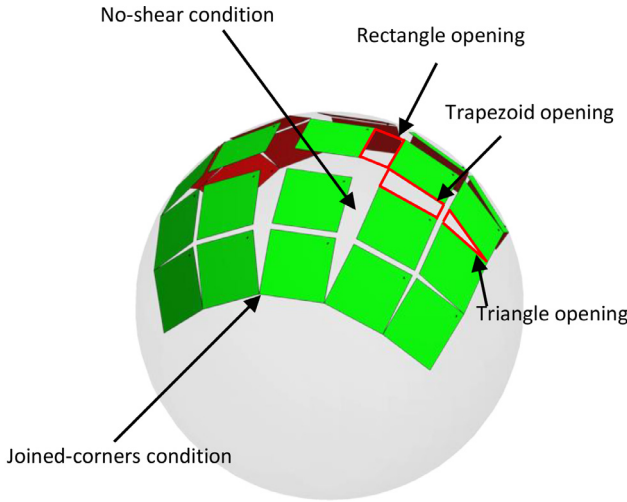


Fig. 2. Arrangement of square tiles on a sphere to achieve the fourth target configuration (spherical).

$$x_0 = \frac{1}{2}, \quad z_0 = \sqrt{R^2 - \left(\frac{1}{2}\right)^2}. \quad (1)$$

Since the tiles form a square grid, we index the tiles on two indices (i, j) , with the $(0, 0)$ th tile located at the “North Pole” of the sphere. For each tile, we define the four corner coordinates in clockwise order, and distinguish them by adding a third index $k \in [1, \dots, 4]$, as illustrated in Fig. 3(a). For the $(0, 0)$ th tile, the four vertices are

$$\mathbf{P}_{0,0,1} = (x_0, x_0, z_0), \quad (2)$$

$$\mathbf{P}_{0,0,2} = (-x_0, x_0, z_0), \quad (3)$$

$$\mathbf{P}_{0,0,3} = (-x_0, -x_0, z_0), \quad (4)$$

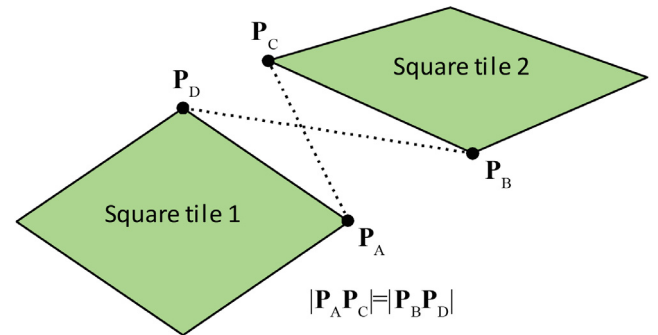


Fig. 4. No-shear condition between adjacent square tiles to reduce design parameters.

$$\mathbf{P}_{0,0,4} = (x_0, -x_0, z_0) \quad (5)$$

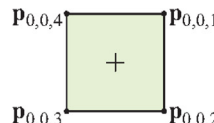
We can construct a local frame of unit vector $(\mathbf{x}_{ij}, \mathbf{y}_{ij}, \mathbf{z}_{ij})$ for each tile, where \mathbf{x}_{ij} points from the center of the tile to the first edge and is perpendicular to it; \mathbf{y}_{ij} points from the center of the tile to the second edge and is perpendicular to it; and \mathbf{z}_{ij} is normal to the tile. For the $(0, 0)$ th tile, the local frame is

$$\mathbf{x} = (1, 0, 0), \quad \mathbf{y} = (0, 1, 0), \quad \mathbf{z} = (0, 0, 1) \quad (6)$$

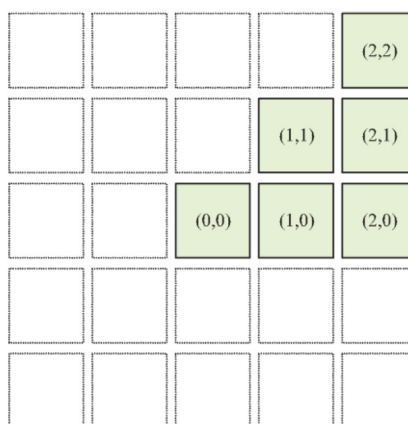
A tile anywhere on the sphere can be parameterized on three angles that describe a transformation of the tile from the position of the $(0, 0)$ th tile:

- ψ_{ij} , an initial rotation of the tile about the z -axis;
- θ_{ij} , an azimuthal rotation of the tile from the North Pole down to a lower latitude;
- ϕ_{ij} , an axial rotation of the tile about the z -axis to a different longitude.

We define the transformation of a vector \mathbf{q}_{ij} in terms of arbitrary $(\theta_{ij}, \phi_{ij}, \psi_{ij})$ by



(a) Labeling of the four vertices of a tile



(b) Schematic of a $(2n + 1) \times (2n + 1)$ array of tiles with indices (i, j) ; only the shaded tiles have independent variables to be solved for

Fig. 3. Labeling of vertices and tiles.

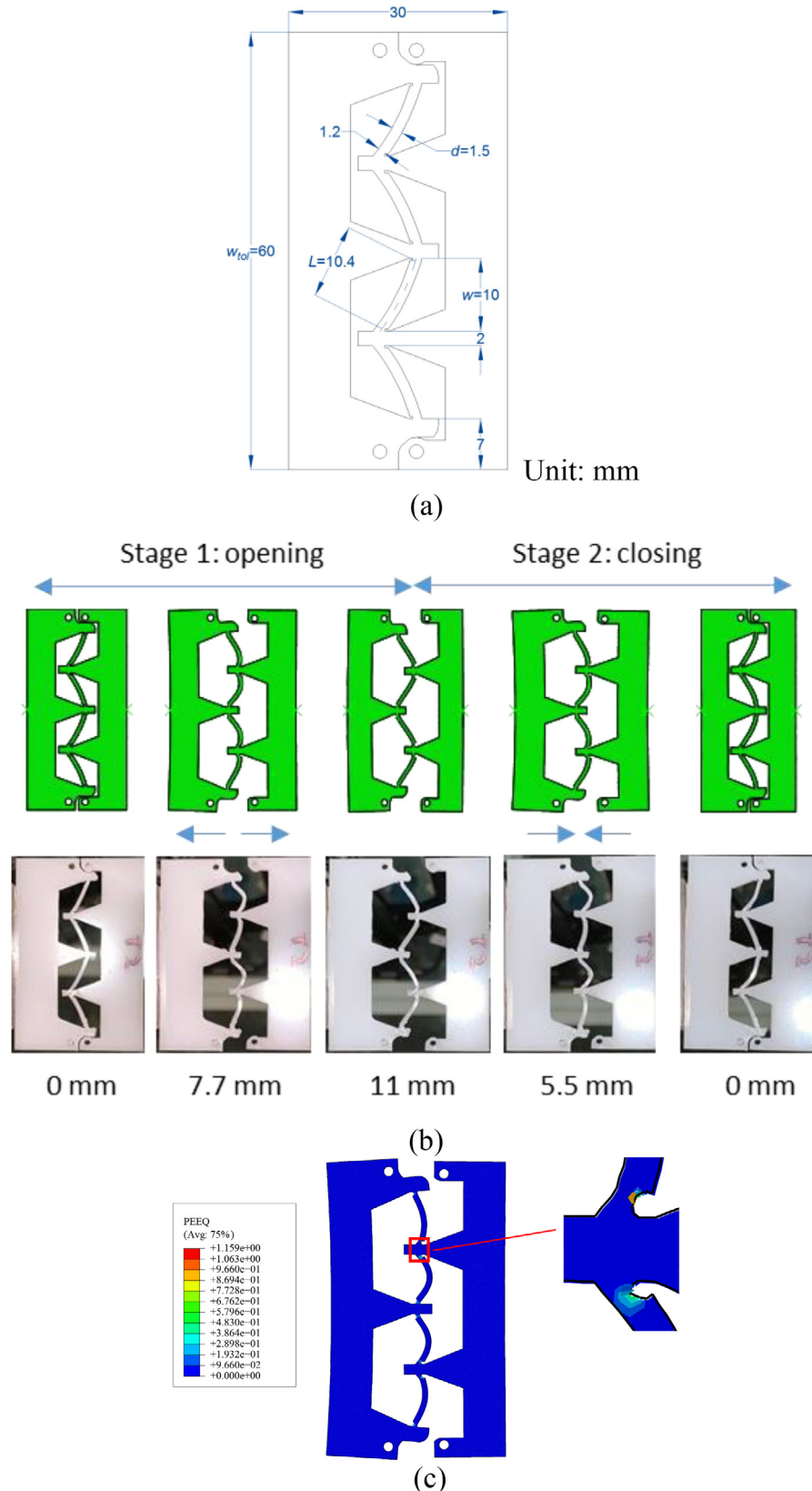


Fig. 5. A rectangle LRBT element: (a) schematic drawing with dimensions, (b) deformation given in numerical simulation and experiment with respective displacements of 0 mm, 6.5 mm, 11 mm, 6.5 mm, and 0 mm, and (c) plastic deformation in the connection hinges that forms living hinges.

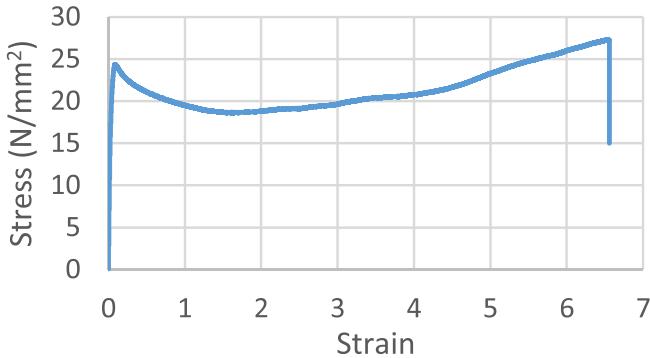


Fig. 6. The uniaxial stress-strain curve of polypropylene copolymer.

$$\mathbf{a}_{ij} = \left(\cos\left(\phi + \frac{\pi}{2}\right), \sin\left(\phi + \frac{\pi}{2}\right), 0 \right), \quad (7)$$

$$\mathbf{n}_{ij} = (\sin \theta \cos \phi, \sin \theta \sin \phi, \cos \theta), \quad (8)$$

$$\mathbf{q}_{ij} = \mathbf{R}(\phi, \mathbf{n}) \cdot \mathbf{R}(\theta, \mathbf{a}) \cdot \mathbf{q}_{0,0}, \quad (9)$$

where $\mathbf{R}(\alpha, \mathbf{u})$ is the 3D rotation through angle α about axis \mathbf{u} . \mathbf{q}_{ij} can represent either a vertex corner vector $\mathbf{P}_{ij,k}$ or a local frame vector \mathbf{x}_{ij} , \mathbf{y}_{ij} , or \mathbf{z}_{ij} .

We can simplify the problem by assuming mirror symmetry along the reflection axes of a square, in which case we only need to solve for a subset of the tiles. If we specify a

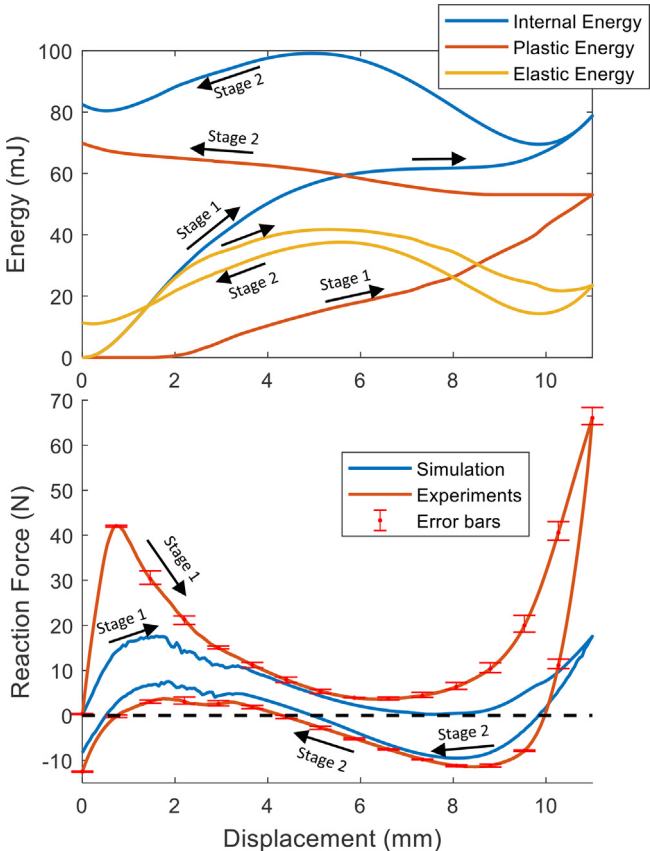


Fig. 7. Plots of energy (from simulation) and reaction force (from simulation and experiments) to the displacement of stage 1 (pulling from 0 mm to 11 mm) and stage 2 (compressing from 11 mm to 0 mm) of a rectangle LRBT joint.

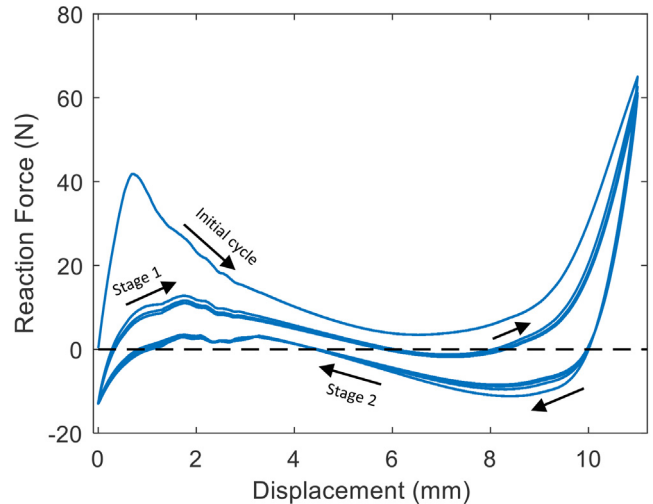


Fig. 8. Plots of the experimental reaction force to the displacement in a cyclic loading (between 0 mm and 11 mm displacement) of a rectangle LRBT joint.

$(2n+1) \times (2n+1)$ array, we need to solve only for the tiles within indices $i = 0, \dots, n, j = 0, \dots, i$, as illustrated in Fig. 3.

We set up the problem of finding tiles positions as a constrained optimization, where the variables being constrained are the three angles for each tile (via the tile corners parameterized on them), and the constraints are of several types (see Fig. 4):

- **Joined corners.** Because we want the largest possible fill factor, we want no excess gaps between tiles. We achieve this by choosing that the corners of adjacent tiles along the outside ring are joined.
- **No shear.** In order to reduce the number of design variables, we adopt the *no-shear* condition on adjacent tiles.

For the joined-corners constraint, a simple constraint that specifies joining would be to require that the distance between the pair of corners to be joined be set equal to zero. However, this is numerically fragile; it is equivalent to finding the zero of a function by minimizing its absolute value. Instead, we should like to find a multidimensional function whose value goes through zero smoothly.

We achieve this by expressing the coordinates of one of the corners to be joined in the local frame of the tile of the other coordinate, and then requiring that the local x and y coordinates match. (There is no need to match the z coordinates because the vertices are already on the surface of the sphere.) Thus, if we denote the two corners to be forced to join by $\mathbf{P}_{i_1 j_1, k_1}$ and $\mathbf{P}_{i_2 j_2, k_2}$, we have two equality constraints to enforce point coincidence:

$$(\mathbf{P}_{i_1 j_1, k_1} - \mathbf{P}_{i_2 j_2, k_2}) \cdot \mathbf{x}_{i_1 j_1} = 0, \quad (10)$$

$$(\mathbf{P}_{i_1 j_1, k_1} - \mathbf{P}_{i_2 j_2, k_2}) \cdot \mathbf{y}_{i_1 j_1} = 0. \quad (11)$$

The no-shear condition arises from the preference to reduce the number of design variables (for arranging squares on a sphere) and regulate the relative motion between square tiles (so that shapes of opening are easier to categorize). If we denote the vertices of the two tiles as $\mathbf{P}_A, \mathbf{P}_B, \mathbf{P}_C$, and \mathbf{P}_D , then the no-shear condition for that particular pair is simply

$$\|\mathbf{P}_A - \mathbf{P}_C\| - \|\mathbf{P}_B - \mathbf{P}_D\| = 0 \quad (12)$$

The joined-corners and no-shear conditions form the constraints of the optimization.

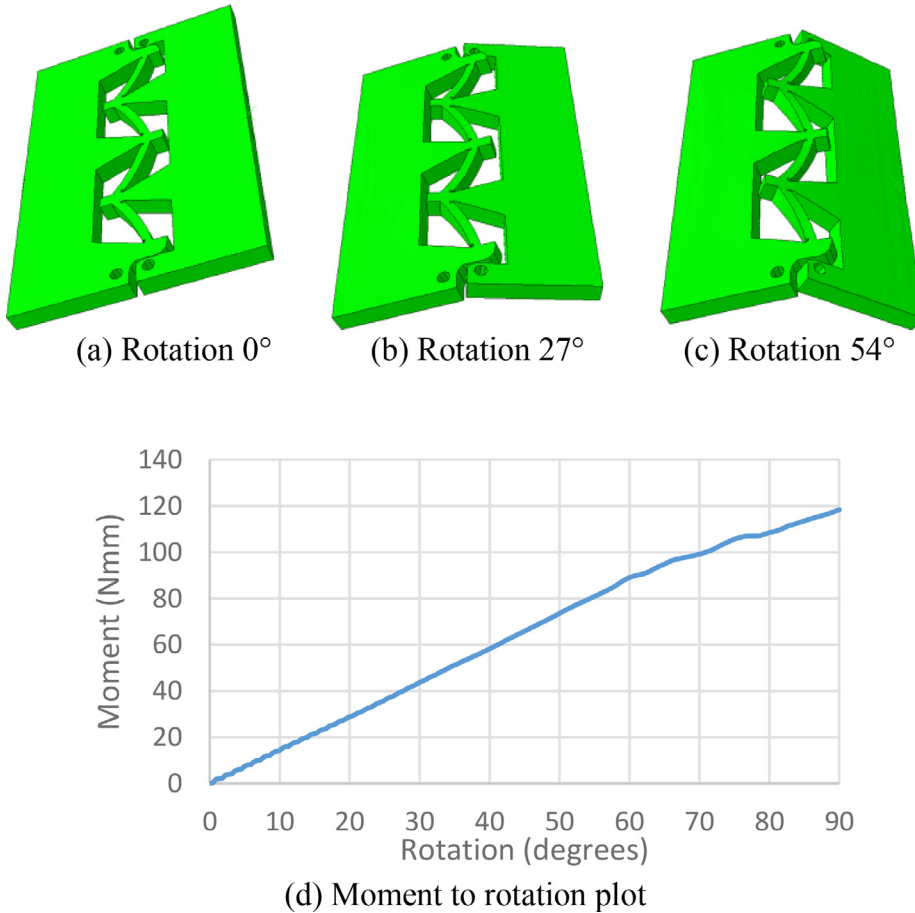


Fig. 9. Simulated bending deformation of a rectangle LRBT element and its moment to rotation plot.

For the figure of merit, we use the goal that we would like the tiles to be as evenly spaced as possible; a way of achieving this is to choose the root mean square (RMS) sum of the distances between adjacent pairs of vertices to be zero (since using RMS sum of spacing of elements confined to a finite region will, all else being equal, drive the spacing to be roughly equivalent). In fact, as it turns out, other constraints of the spherical geometry force distinctly unequal spacing, but choosing the RMS goal has the effect of “soaking up” any excess degrees of freedom in the system, leading to a definite (numerical) solution for the positions.

We optimize over the angle variables $(\theta_{ij}, \phi_{ij}, \psi_{ij})$ for the (i,j) values of the tiles in the minimal set, using symmetry to find the coordinates for any other tile vertices involved in the constraints or figure of merit. Note that the positions of the joined corners are not placed: they are determined from the solution of the system of equations. There is no guarantee of a solution; for any given number of tiles, there is a minimum sphere size for which a solution can be found. (This is obvious from the fact that at some point, the area of the sphere is going to be less than the area of the set of tiles.)

We parameterize each tile in terms of three variables: the altitude and azimuth of the centroid of the tile and the relative rotation of the tile about its centroid. An overall design parameter is the sphere radius (we assume unit square tiles). From those parameters, we can compute the four vertices of each tile; from the vertices, we can construct our FOM and the no-shear and joined-corner condition constraint equations. We then solve this system of equations (using *Mathematica*) to find the tile arrangement shown in Fig. 2, and this method is used in the rest of this paper.

The resultant openings between square tiles can be categorized as rectangle, triangle, and trapezoid shapes as shown in Fig. 2. Bistable-translational elements were then designed accordingly, as described in the next section.

3. Introduction of Linear-Rotational and Bistable-Translational (LRBT) joints

In this section, joints that connect square tiles that can in one hand provide rotation along the edge of squares for isometric transformation, as shown in Fig. 1(a)–(c), and in the other hand can provide translation between squares for metric-changing transformation, as shown in Fig. 2, are introduced. They are categorized into rectangle, triangle, and trapezoid openings based on their target open shapes.

3.1. The rectangle opening LRBT joints

3.1.1. Geometry and deformation

Consider two plates that are connected by four slightly curved elastic beams in 2D, as shown in Fig. 5(a), where end connections of those beams have thinner profiles so that rotation can occur easily. The out of plane thickness of the material $t = 3.175$ mm. The material used is polypropylene copolymer. Tensile tests were performed, and the material stress-strain curve is given in Fig. 6. The properties of the polypropylene copolymer are as follows: density = 10^{-3} g/mm³, Young's modulus = 322 MPa, Poisson's ratio = 0.3, yield stress = 24 MPa, yield strain $\varepsilon_y = 7.5\%$, and the elongation before break is 650%.

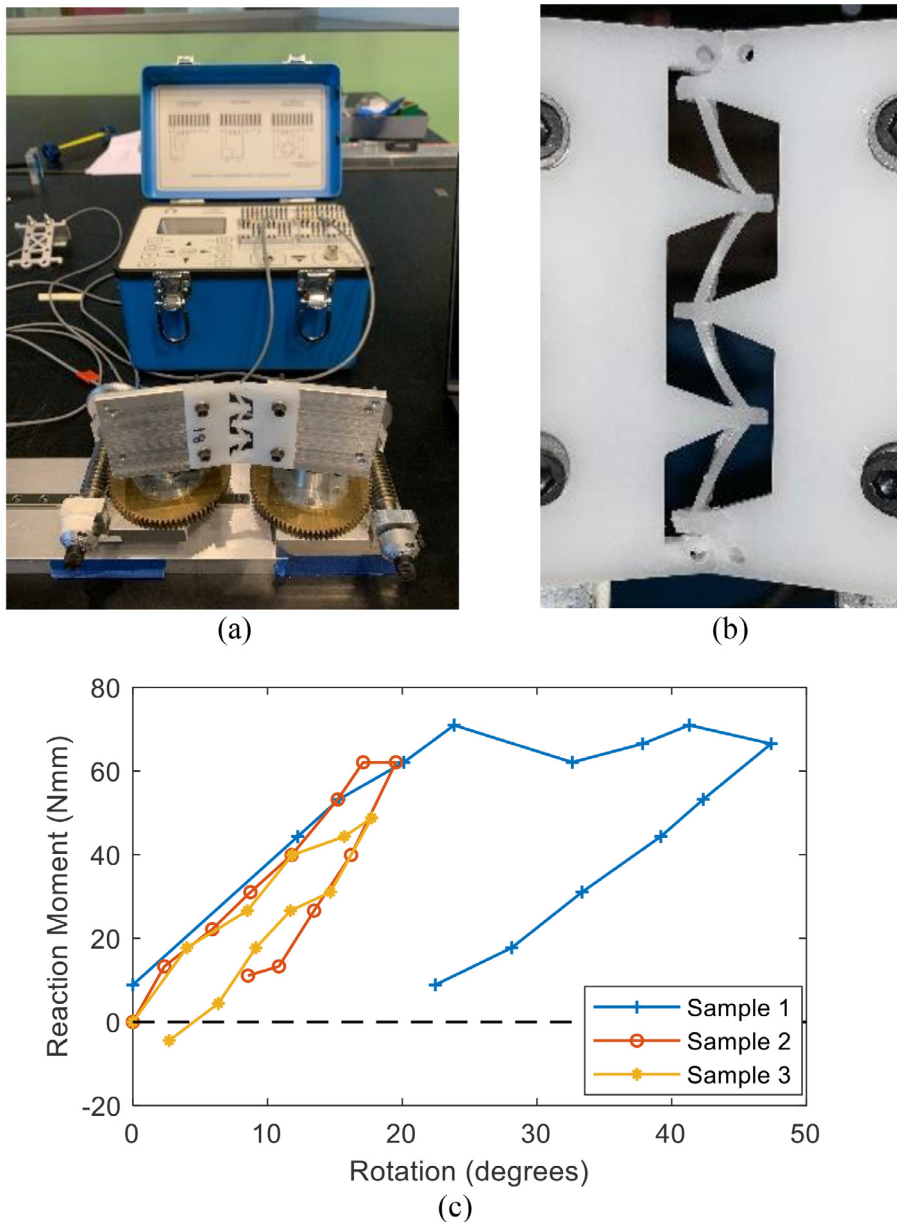


Fig. 10. Bending experiments of 3 rectangle LRBT samples: (a) the experimental setup; (b) deformation with a rotation of 40°; and (c) moment to rotation plots.

3.1.1.1. Bistability in translation. The in-plane translational (extensional and compressional) behavior of LRBT hinges was modeled in Abaqus/Explicit (Abaqus, 2013) using 85,736 C3D8R elements. A convergence test of mesh density was conducted, and the kinetic energy and artificial energy of all simulations were well below 5% of the total energy. Linear elasticity and plasticity (input the curve in Fig. 6 into Abaqus) were considered in the material model. Viscosity of the material was not included because simple material tests (without varying and recording strain rates) were employed as the numerical model is to only capture the main feature (the LRBT effect) of the joint. In the simulation, the left side of the structure was clamped, and a horizontal displacement was imposed to the right side of the structure. The prescribed displacement was 11 mm applied over a 0.5 s interval. This is noted as stage 1, in which the structure was pulled open as shown in Fig. 5(b). The displacement was then reversed back to 0 mm over 0.5 s; this is noted as stage 2. In these two stages, plastic deformation only occurred in

the joining area to form living hinges while the rest of the beams remained elastic, as shown in Fig. 5(c).

The same displacement was imposed experimentally by an Instron machine with a speed of 5.5 mm/min. The experimental deformation is shown in Fig. 5(b). Three test samples were manufactured by laser cutting a 3.175 mm thick polypropylene sheet.

Energy and reaction force plots of this process are given in Fig. 7. As shown in Fig. 6, the material is softened in the plastic region. This is reflected in Fig. 7, where the plastic energy is flatter in stage 2 when the displacement is decreasing. This indicates that localized and soft plastic living hinges are formed in the end connections of those beams (noted in Fig. 5(c)). In consequence, two stable states can be observed in stage 2 according to internal energy, elastic energy, and reaction force. The slight deviation of stable positions between internal energy (or reaction force) and elastic energy is due to the existence of plastic

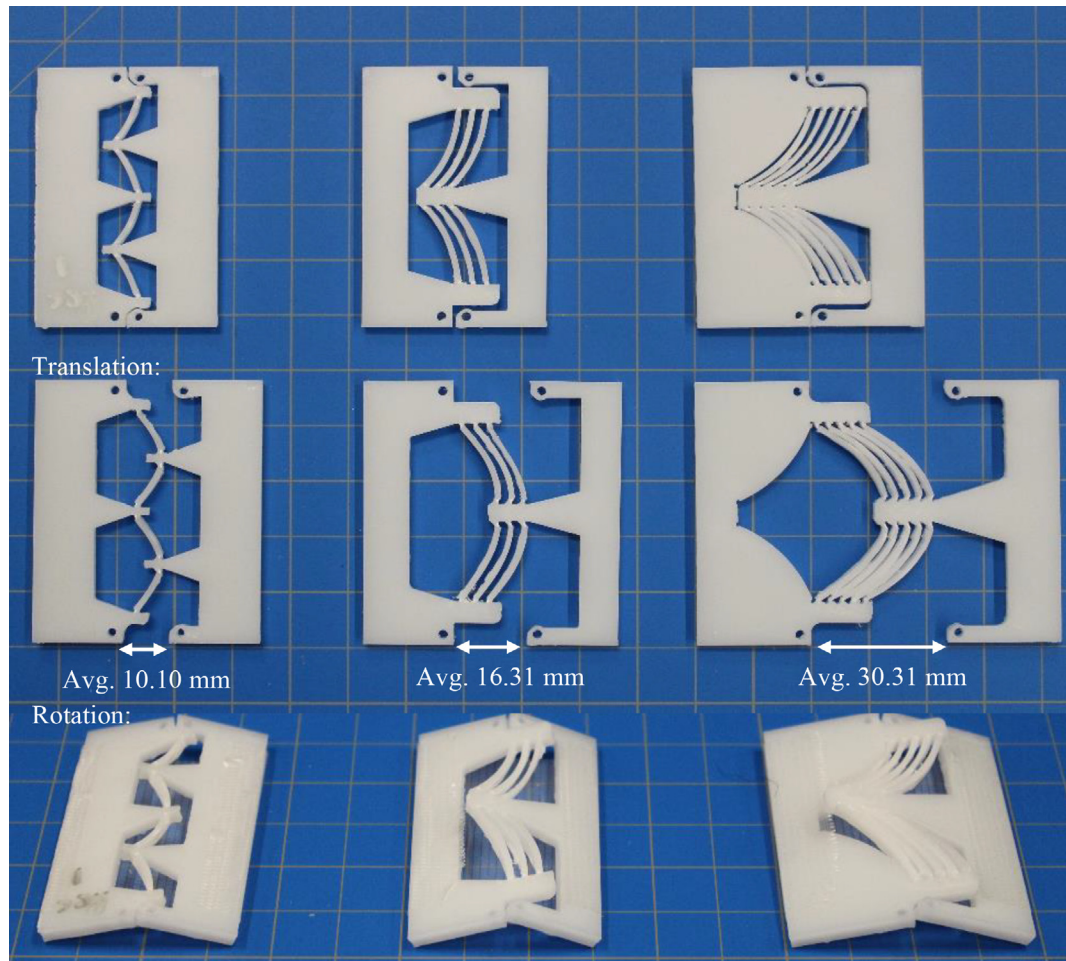


Fig. 11. Three rectangle LRBT joints and their translational and rotational deformations.

Table 1

Three rectangle LRBT joints.

Target Opening g_r	10 mm	17 mm	32 mm
Design			
Opening size exp. (mm)	10.10	16.31	30.31
Avg. exp. error	1.02%	-4.07%	-5.30%
Num. translation (stage 2) and bending plots	Bending Rotation (degrees) Reaction Moment (N/mm) Translational Displacement (mm)	Bending Rotation (degrees) Reaction Moment (N/mm) Translational Displacement (mm)	Bending Rotation (degrees) Reaction Moment (N/mm) Translational Displacement (mm)

hinges (residual moments). As a result, the structure (after the formation of plastic living hinges) is bi-stable in the translational deformation. Both stable configurations occur when the elastic

beams are undeformed (with slight drifting due to plastic hinges). Plots of numerical and experimental reaction forces in Fig. 7 show almost identical stable positions in stage 2. Experi-

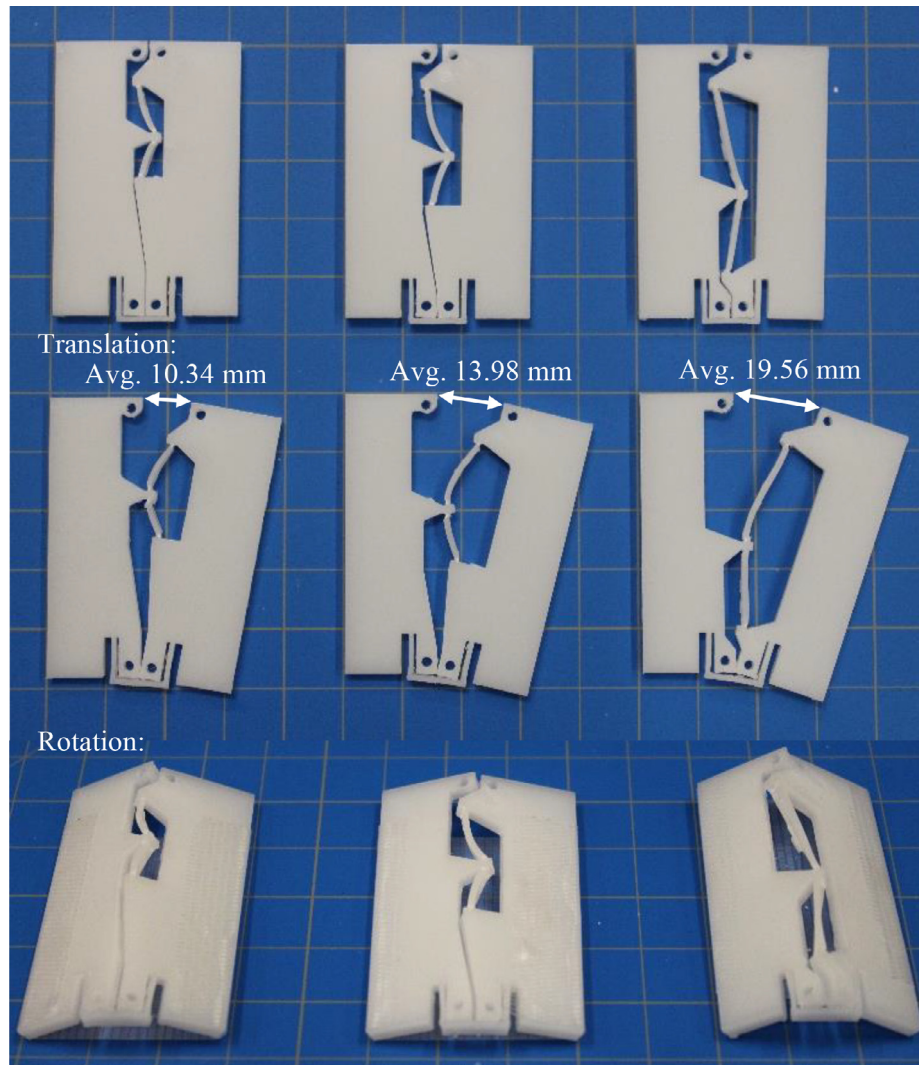


Fig. 12. Three triangle LRBT joints and their translational and rotational deformations.

Table 2
Three triangle LRBT joints.

Target Opening g_t	9.8 mm	14.1 mm	20.5 mm
Design			
Opening size exp. (mm)	10.34	13.98	19.56
Avg. error	5.51%	-0.89%	-4.59%
Num. translation (stage 2) and bending plots	 Bending Rotation (degrees) Reaction Moment (Nmm) Translational Displacement (mm) Elastic Energy (mJ)	 Bending Rotation (degrees) Reaction Moment (Nmm) Translational Displacement (mm) Elastic Energy (mJ)	 Bending Rotation (degrees) Reaction Moment (Nmm) Translational Displacement (mm) Elastic Energy (mJ)

Table 3

Five trapezoidal LRBT joints.

Target Opening g_1 and g_2	14.3 mm 9.8 mm	16.7 mm 15.1 mm	23.5 mm 14.1 mm
Design			
Opening size exp. (mm)	13.97 9.88	15.70 15.08	21.37 13.51
Avg. error	-2.34% 0.77%	-6.02% -0.17%	-9.06% -4.22%
Num. translation (stage 2) and bending plots			
Target Opening g_1 and g_2	29.7 mm 25.5 mm	30.1 mm 21.2 mm	
Design			
Opening size exp. (mm)	28.03 22.74	27.96 22.43	
Avg. error	-5.64% -10.84%	-7.11% 5.78%	
Num. translation (stage 2) and bending plots			

mental reaction forces of the three samples show good consistency as noted by the error bars. However, they have overall different magnitude to the numerical reaction force in Fig. 7(b). The difference is significant in stage 1 where plastic living hinges are in the process of forming which is not well captured by the simulation, while stage 2 shows a closer match. The experimental reaction force at the displacement of 11 mm is significantly the highest, which indicates the beams are practically shorter than the design due to manufacturing inaccuracy and the effect of beam width. As a result, the beams are in tension at the displacement of 11 mm in experiments, and the plot shows a sharp increase of reaction force. Additionally, the lack of consideration of viscous effects in the numerical model can also contribute to this deviation (Fig. 8).

Cyclic loading (with 4 cycles in total and the same speed) was tested experimentally and has shown that the sample is repeatedly bistable after the first half of the initial cycle where plastic hinges or living hinges (noted in Fig. 5(c)) are formed. Differences

between the reaction forces of stage 1 and 2 were mainly caused by viscoelasticity.

Elastic energy during the stage 2 in the numerical simulation captures the inherent bistability better than the internal energy which includes the plastic energy that shifts the stable positions differently depending on the loading history/direction. In consequence, elastic energy is used in later sections to characterize the translational bistability of other LRBT joints.

3.1.1.2. Linear elastic in rotation. Consider the same structure given in Fig. 5(a). Now, pure bending is applied in the numerical simulation, where the plate on the left side is clamped, and the rotation is applied to the plate on the right side, as shown in Fig. 9. The total step time is 0.5 s. The hinge is linear elastic until the rotation reaches 60°, where plasticity starts to occur, as shown in Fig. 9(d). This result indicates that this structure (if made of linear elastic material) shall have linear elastic bending behavior.

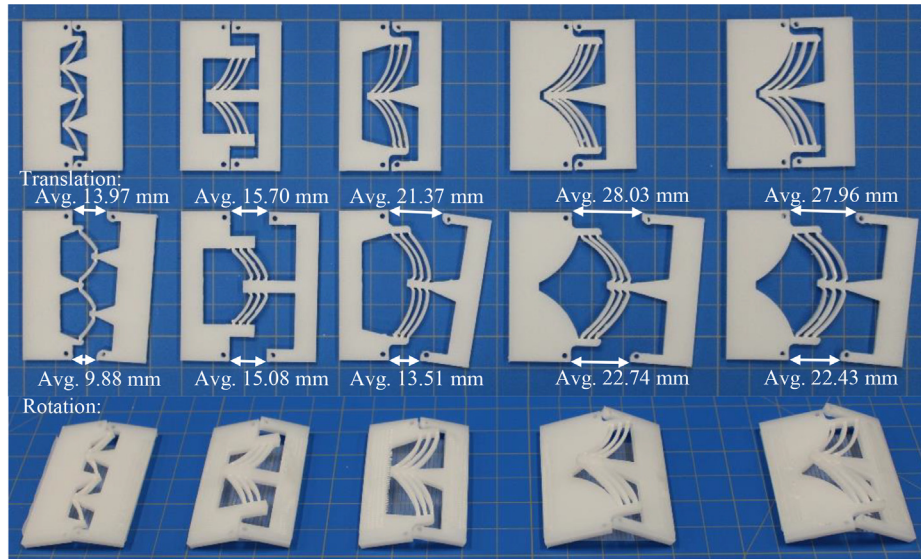


Fig. 13. Five trapezoidal LRBT joints and their translational and rotational deformations.



Fig. 14. Arrangement of 5 by 5 square tiles with 60 mm width on a sphere with radius 168 mm, and there are 6 different positions of square tiles (based on symmetry) that are marked by numbers.

Table 4

Opening sizes between adjacent square tiles measured from the arrangement of squares in Fig. 14.

Pair of Square Tiles	Opening Type	Opening Size (mm)
1–2	Rectangle	32.5
2–3	Rectangle	2.9
2–4	Trapezoidal	$g_1 = 30.1$ $g_2 = 21.2$
3–5	Triangle	20.5
4–5	Trapezoidal	$g_1 = 3.8$ $g_2 = 3.0$
5–6	Triangle	3.7

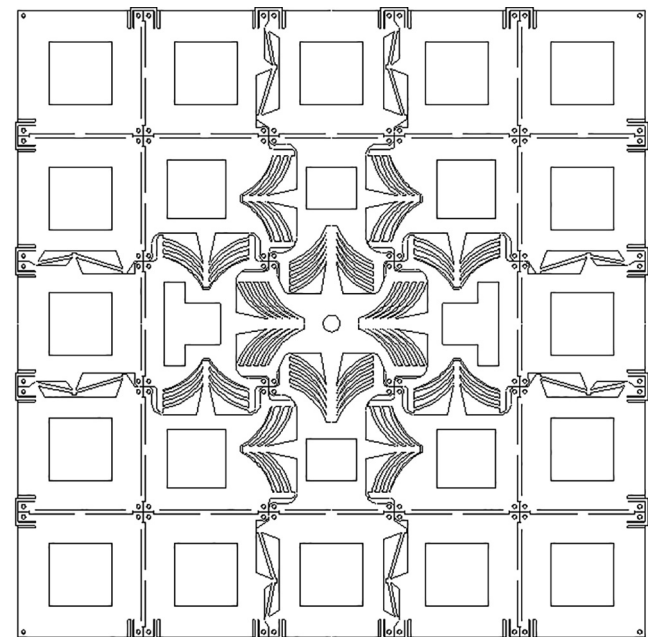


Fig. 15. The 5 by 5 cutting pattern of the resultant structure that can reconfigure to all 4 target configurations presented in Fig. 1.

Experiments of 3 samples were conducted using a pure bending machine (with a accuracy of 8.9 Nmm) that has been introduced and used in (Leclerc, et al., 2017; Ferraro and Pellegrino, 2018). The experimental setup is shown in Fig. 10(a), experimental bending deformation with a rotation of 40° is given in Fig. 10(b), and plots of reaction moments of 3 samples are presented in Fig. 10(c). After the experiment, sample 2 and 3 slowly recovered to the flat configuration while sample 1 recovered to a residual rotation of 7°. This recovery together with plots indicates that the structure is viscoelastic within a rotation of 25°.

This linear elastic behavior shows that this rectangle LRBT joint works similarly to a LET joint (Jacobsen, 2009). (A LET joint is a torsional hinge with integrated beams that act as torsional springs

whose stiffness is designable and governed by geometric parameters of the beams.) Numerical simulation with the same settings (mesh density, loading speed, etc.) is used in [Sections 3.1.2, 3.2, and 3.3](#) and to characterize the bending behavior of other LRBT joints with a linear elastic material assignment.

The hinge-rotation does not remove the translational bistability and does not introduce parasitic translational deformation. This is observed in experiments and simulations, where the hinge stayed closed stably during hinge-rotation. Translation of the hinge is associated with bending deformation of beams, while rotation of the hinge is associated with torsional deformation of beams. Intuitively, the translational bistability is introduced by the two symmetric configurations (open and closed in translation) where beams are almost “bending-free”. The introduction of hinge-rotation does not break that symmetry so the bistability remains. Hinge-rotation creates torsional deformation in beams, which has a negligible translational projection. As a consequence, parasitic translational deformation is not expected during bending.

Now we have presented a basic element that can act as a bistable translational spring or a linear torsional hinge depending

on the loading. These two behaviors (translating and bending) are well separated by the energy barrier shown in the stage 2 of [Fig. 7](#).

3.1.2. Parametric study

To develop design guidelines for LRBT hinges, the following design requirements are proposed and need to be satisfied: (a) beams are not plastically deformed; (b) reasonable stiffness for the bistability which is realized by introducing small initial curvature to beams; (c) the translational deformation (snap-through of beams) remains in 2D, which is achieved by designing beam widths significantly smaller than the material thickness. A rough analytical model is used to prevent plasticity in the beams during translation (except at the ends of the beams). Assuming the beam deforms into a circular arch, geometric parameters w , L (taken as the distance between end points), and d noted in [Fig. 5](#) need to satisfy the following relationships for it to stay within the elastic region (to satisfy requirement (a)).

$$\sin\left(\frac{\theta}{2}\right) = \frac{w}{2R} \quad (13)$$

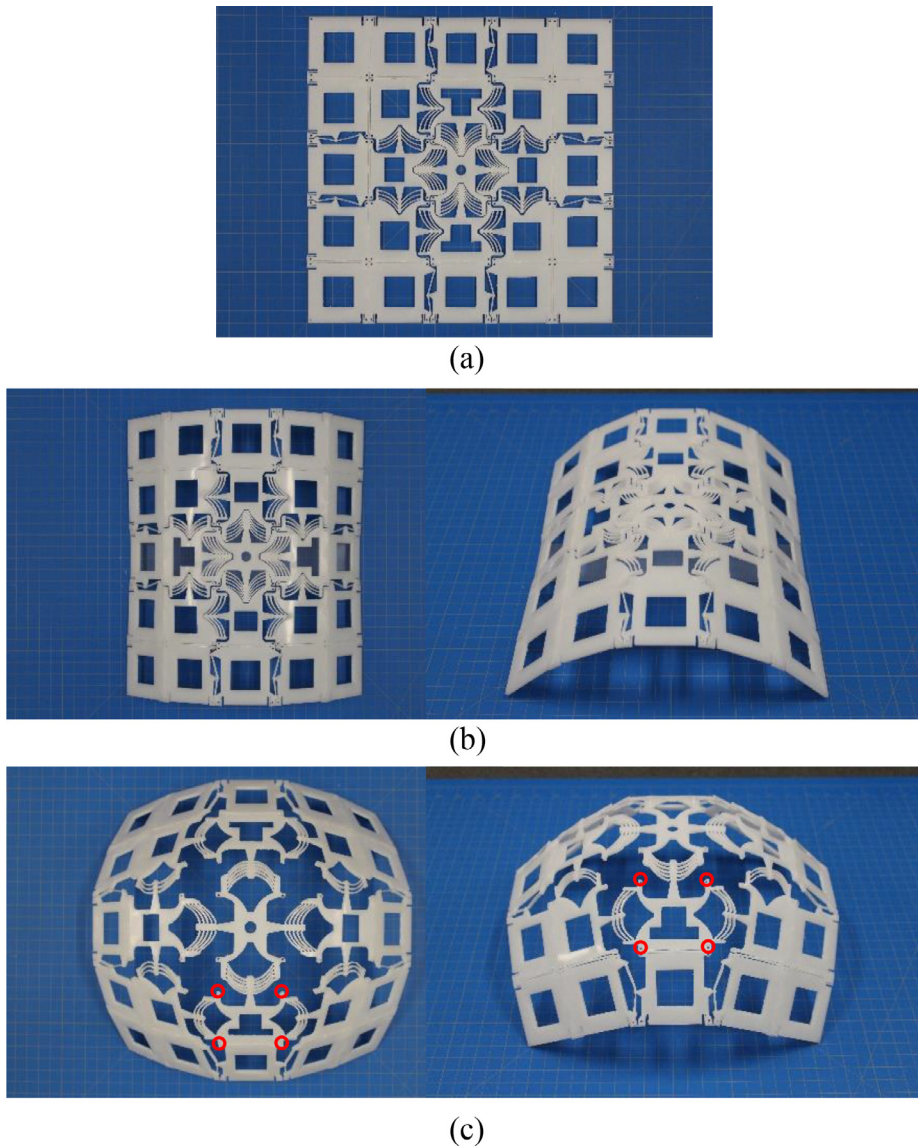


Fig. 16. The 5 by 5 reconfigurable surface in (a) flat configuration (stable), (b) cylindrical configuration (held stable by tape), and (c) spherical configuration (stable).

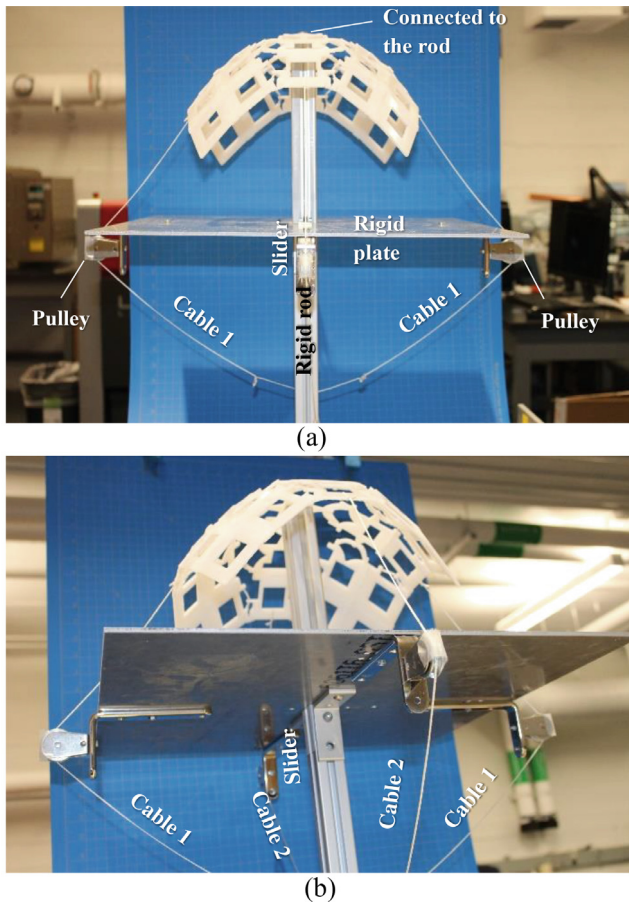


Fig. 17. The actuation setup that consists of 2 cables and 1 slider in (a) side view and (b) bottom view.

$$L = R\theta \quad (14)$$

$$R > \frac{d}{2\varepsilon_y} \quad (15)$$

where R and θ are the radius and the central angle of the deformed beam, respectively. This model provides a rule of thumb for design, and has not considered viscosity and used simple engineering strain as the indication of yielding. For the material thickness $t = 3.175$ mm used in this study, a beam width $d = 1.5$ mm (to satisfy requirement (c)) and total width $w_{tol} = 60$ mm (to match the antenna tile size) as noted in Fig. 5(a) are chosen for all LRBT designs in this paper.

Drawing procedures for generating rectangle LRBT joints with specified openings are given in Fig. 24 in Appendix A. Designs of three different target rectangle openings g_r , which are 10 mm, 17 mm, and 32 mm are provided in Table 1 according to the principle introduced in Fig. 24. Similar designs that are used for the 17 mm and 32 mm openings are previously introduced in (Gomm et al., 2002), which have several pairs of beams in the transverse direction of the hinge to eliminate “parasitic” kinematics illustrated in (Delimont et al., 2015). All three design requirements are satisfied.

Two samples of each LRBT hinge design were manufactured by laser cutter, and the averaged stable opening sizes are given in Table 1. Manufactured samples are presented in Fig. 11, which shows the translational deformation (stable by elastic strain energy) and rotational deformation (held at a fixed rotation angle by tape). They open to approximately the designed size and rotate along the edge of two plates. Slight deviations from the target openings are mainly caused by (1) the occurrence of the plastic hinges is not at ends of beams so that effective beam lengths are smaller and (1) deformation of elastic beams due to residual moments at the plastic connection hinges at ends of beams. Drawings with detailed dimensions are given in the supplementary

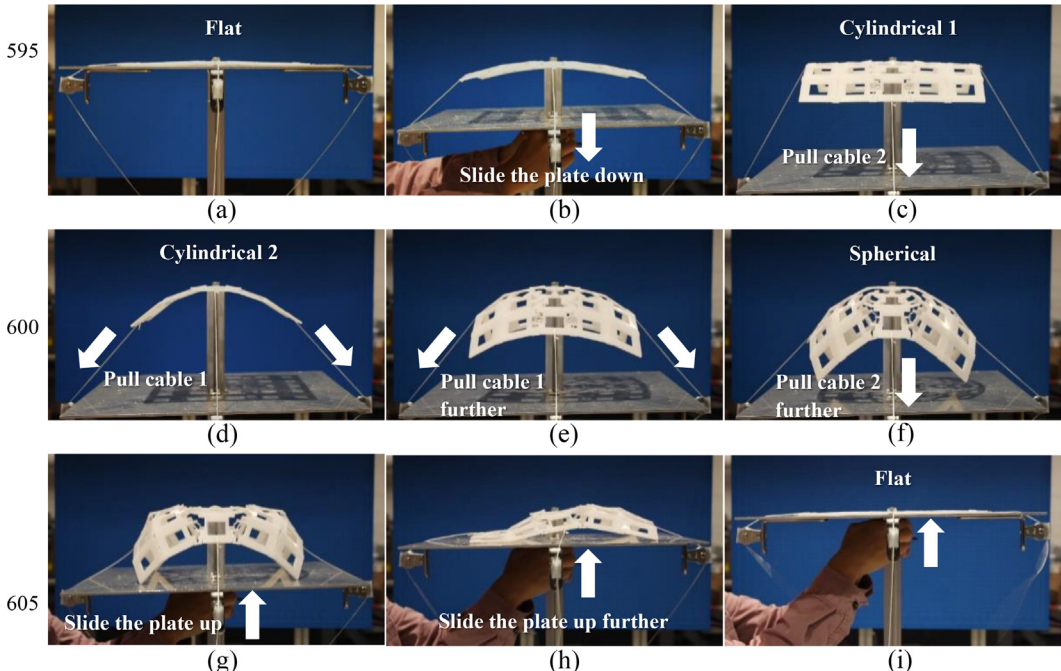


Fig. 18. Morphing in between 4 target configurations by actuating 2 cables and 1 slider.

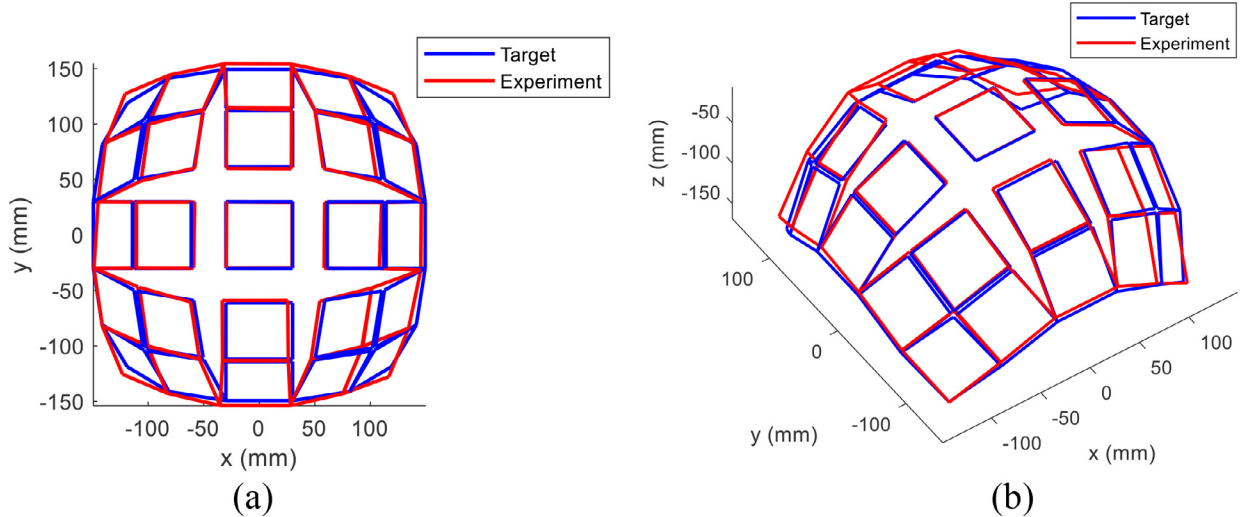


Fig. 19. Comparison of 3D scanned spherical shape and the target shape in (a) top view and (b) side view.

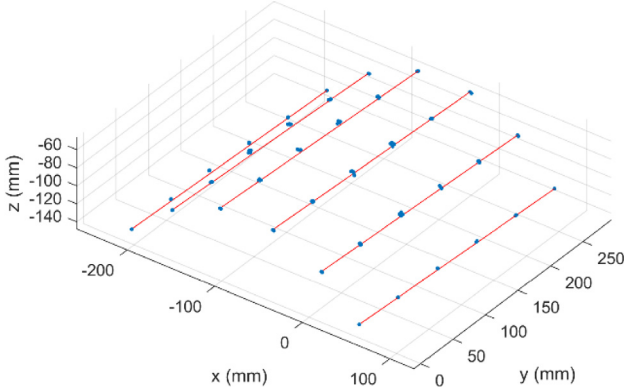


Fig. 20. The 3D scanned cylindrical shape is represented by blue dots, and red ruling lines are to help discern the shape.



Fig. 21. Arrangement of 7 by 7 squares on a sphere.

material. The “kerf” of the laser cutting is 0.2 mm and has been taken into account. Translational (stage 2) and bending plots from numerical simulations are given in [Table 1](#), which shows the linear-rotational and bistable-translational behavior for all three designs. Local fluctuations in curves are due to contact between boundaries during gap closing. Stage 2 (in [Fig. 7](#)) of their translational behavior (compression) is plotted, so the elastic energy is not zero when the translational displacement is zero due to the residual moment in the plastic living hinges.

3.2. The triangle LRBT joints

As shown in [Section 2](#), some target hinge openings are triangle shapes. Drawing procedures for generating triangle LRBT joints with specified openings are given in [Fig. 25](#) in Appendix A. The bottom corners of the plates must be connected while still allowing in- and out-of-plane rotation. This can be achieved by connecting the bottom corners with cutout beams as shown in [Fig. 12](#) and [Fig. 25\(c\)](#), producing a compliant pin-joint connection. Three designs are given in [Table 2](#) and [Fig. 12](#). Plots from numerical simulations show that they are linear-rotational and bistable-translational.

3.3. The trapezoid LRBT joints

Some target openings take trapezoidal shapes. Drawing procedures of generating trapezoid LRBT joints with specified openings are given in [Figs. 26](#) and [27](#) in Appendix A. Designs with different openings are presented in [Table 3](#) and [Fig. 13](#). A maximum error of 10.84% is observed. The designs are linear-rotational and bistable-translational as observed in plots of numerical simulations, where the translational displacement is measured as the average of g_1 and g_2 .

This section has presented designs of LRBT joints that can provide the specified opening (rectangular, triangular, or trapezoidal shape) and verified that they are linear elastic in rotation and bistable in translation.

4. Integration into reconfigurable surfaces

Two square (tile) arrangements, 5 by 5 and 7 by 7, were produced using the technique introduced in [Section 2](#). Corresponding

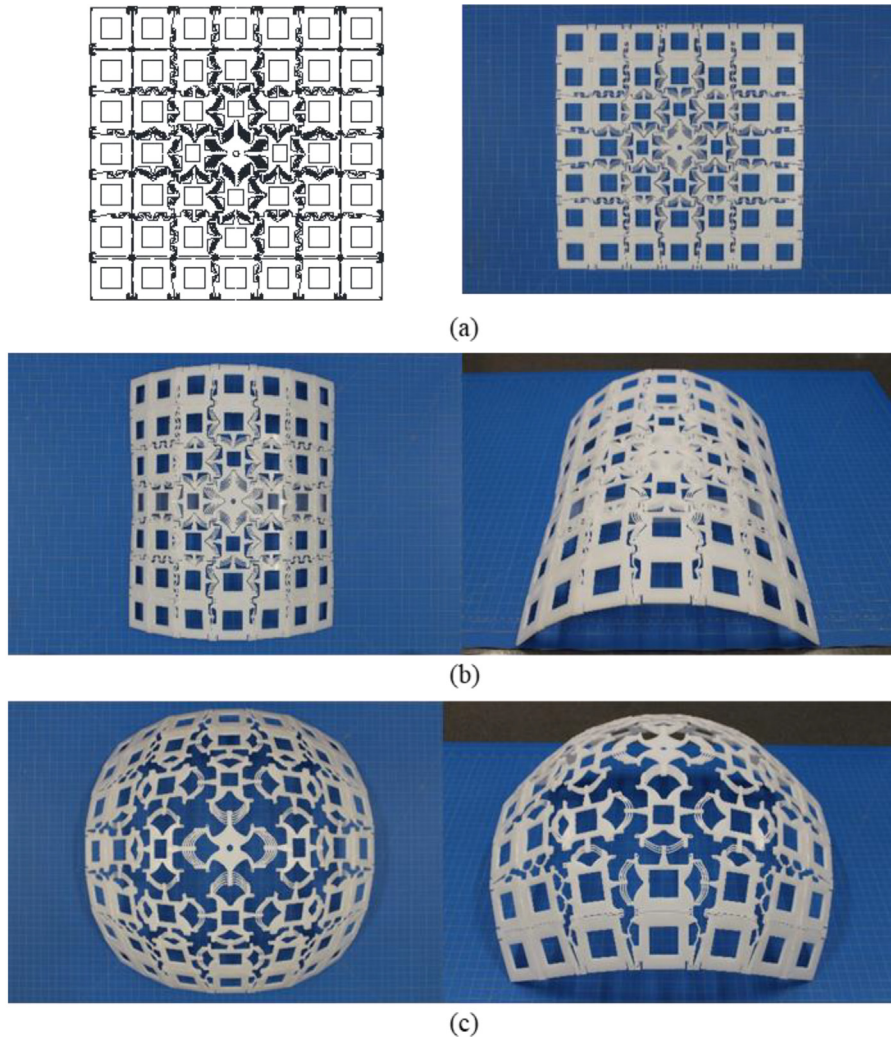


Fig. 22. The 7 by 7 reconfigurable surface in (a) flat, (b) cylindrical, and (c) spherical configurations.

LRBT joints were designed and put into arrays to form the 2D cutting patterns. A laser cutter was used to cut the structures from 3.175 mm thick polypropylene copolymer sheets. An actuation setup was developed to morph the prototype between all 4 target configurations using 3 actuators (2 cables and 1 slider). To characterize the target shapes of the prototype, 3D scanning was used, showing close agreement with the ideal target shapes. High resolution pictures and actuation videos can be found in the [supplementary material](#).

4.1. The 5 by 5 pattern

4.1.1. Arrangement of square tiles on a sphere and the 2D cutting pattern

A 5 by 5 pattern with square size of 60 mm and radius of 168 mm is generated and shown in Fig. 14 where different square tiles are marked with numbers. Openings between each pair of square tiles are given in Table 4 and corresponding joints are chosen from Tables 1–3. A 2D cutting pattern can be generated as shown in Fig. 15 where there are 4 holes at corners of each square for mounting antenna tiles. The widths of some hinge openings are approximately the thickness of the material, so they are jointed simply by torsional beams (LET joints) as almost no translational movement is needed. Redundant material is cut away to save weight. The outcome is one continuous structure.

4.1.2. Manufacturing, Actuation, and shape measurement

It took about 2 h to cut the structure, which produced the reconfigurable surface shown in Fig. 16. The structure in the flat configuration is like an elastic plate which can be folded along the edges of square tiles. It is stable by internal energy at flat and spherical configurations (Fig. 16(a),(c)) and can be stable at cylindrical configurations by actuation (which is taped at the back of the structure in Fig. 16(b)). The out-of-plane stiffness of the structure at flat configuration is provided by the rigid plate (that it conforms to at the back) and contacts introduced by antenna tiles (to be installed at the front). Prestress is created at cylindrical and spherical configurations due to bending deformation of all LRBT joints, which increases the out-of-plane stiffness of the structure. Thicker substrates introduce larger prestress and correspondingly larger stiffness.

Actuation setup was developed and shown in Fig. 17. There are three actuators, including 2 cables and 1 slider. A rigid plate holding 4 pulleys supports the two cables. The plate can slide along a rigid rod (a T-slotted framing rail). The center square tile of the reconfigurable surface is connected to the top of the rigid rod, and the bottom of the rod is clamped to the foundation.

Actuation is shown in Fig. 18. Here, the structure morphs in between 4 target configurations by actuating 2 cables and 1 slider. In the flat configuration (Fig. 18(a)), the structure conformed to the shape of the rigid flat plate. When lowering the rigid plate and

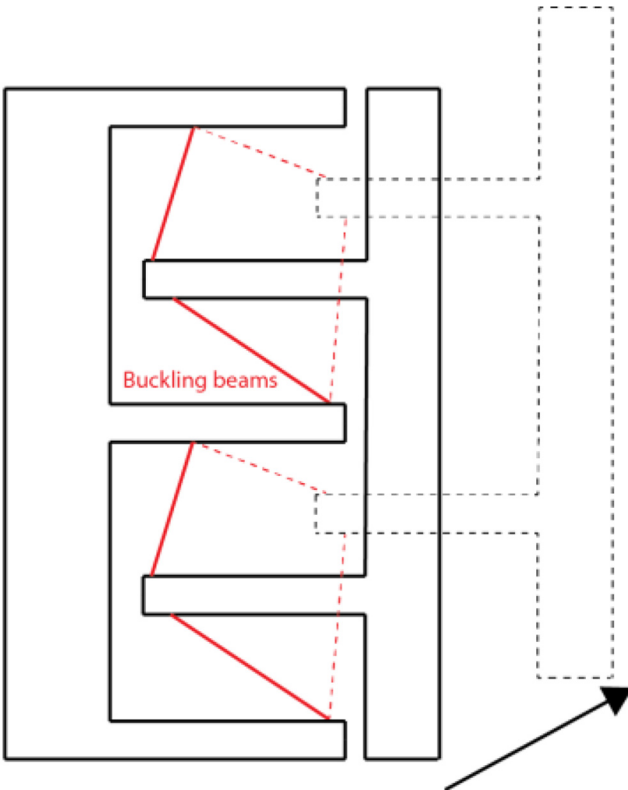


Fig. 23. A LRBT joint that has translation containing “shear” along the hinge direction.

pulling 1 cable (and holding it), cylindrical configurations (Fig. 18(c),(d)) could be achieved where LRBT joints worked as elastic torsional hinges. While pulling 2 cables further, all LRBT joints were snapped open, forming the spherical configuration (Fig. 18(f)). In this configuration, the structure was stable by itself (the cables

did not need to held). Then, sliding the rigid plate up, the structure was compressed between the top of the rigid rod and the top surface of the rigid plate, which closed all the LRBT joints and the structured snapped to the flat configuration (Fig. 18(g)–(i)). A video of the actuation sequence is provided in the [supplementary material](#).

The spherical shape was measured by 3D scanning and was compared to the target shape, which is shown in Fig. 19. Four corners of each square tile, which are circled in red for one square tile in Fig. 16(c), were regarded as reference points and measured. As shown in Fig. 19, the experimental configuration is slightly longer in y direction and shorter in x direction. Four corners of the structure are slightly bulged out compared to the target shape. The maximum deviation (in terms of the distance) from the target coordinate is 14.04 mm, and the averaged deviation is 6.22 mm. The width of the ideal structure is 300 mm, giving a maximum relative error of 4.7% and an averaged relative error of 2.1%. The 3D scanned cylindrical configuration is given in Fig. 20 where good uniformity is observed. The experimental shape can be influenced by the residual stress in the elastic beams, self-weight, plasticity induced during actuation, and manufacturing imperfections.

4.2. The 7 by 7 pattern

The generality of the LRBT design process is demonstrated by constructing a structure composed of a 7 by 7 array of tiles. Fig. 21 shows the 7 by 7 square arrangement on a sphere with tile width of 60 mm and radius of 240 mm. Corresponding LRBT joints can be designed and placed into a 2D array as shown in Fig. 22(a). Cylindrical and spherical configurations are presented in Fig. 22(b) and (c) which visually show good consistency (see Fig. 23).

5. Conclusion

This paper has proposed a new class of reconfigurable surfaces consisting of rigid elements (tiles) connected by novel compliant joints. These joints can work as torsional hinges that enable

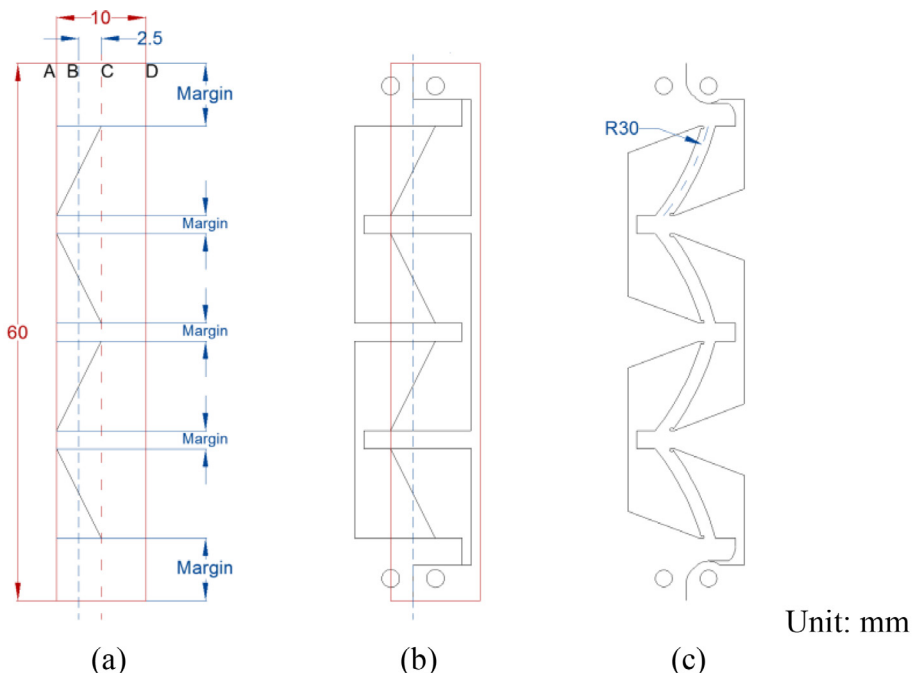


Fig. 24. The drawing procedure of a LRBT joint to match a given rectangle opening and center of rotation.

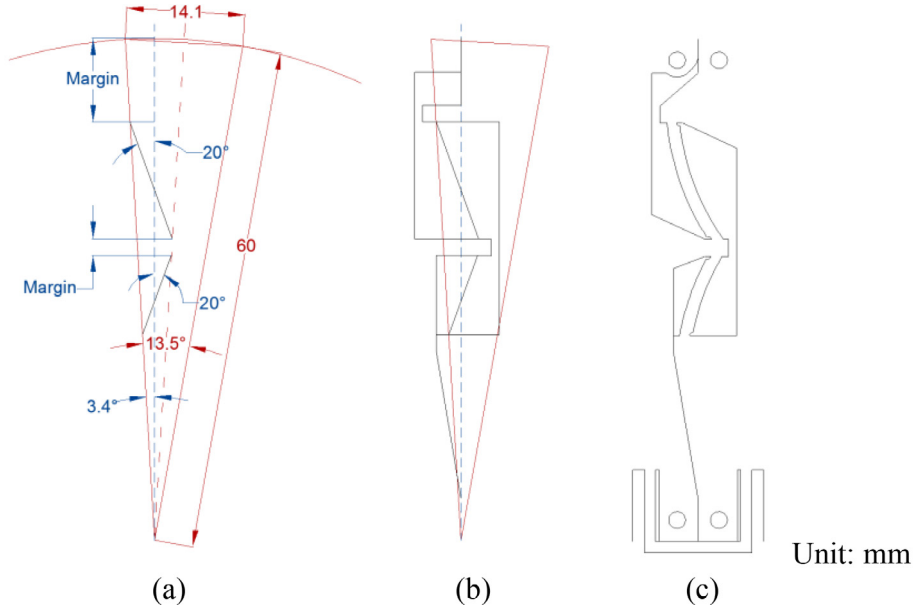


Fig. 25. The drawing procedure of a LTBT joint to match a specified triangle opening and the center of rotation.

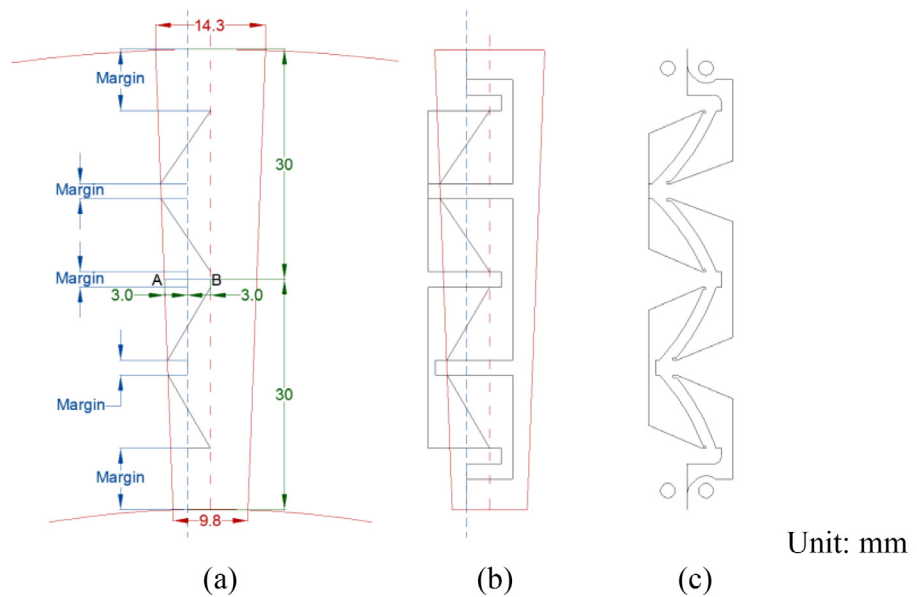


Fig. 26. The drawing procedure of a LTBT joint to match a given small trapezoidal opening and center of rotation.

isometric transformation, such as origami folding, between connected rigid pieces. When actuated specifically, these joints can work as bistable translational springs that bring metric-changing transformation between connected rigid pieces. When the bistability of joints is designed accordingly, desired metric-changing configurations, such as specified spherical shapes, can be achieved with simple actuation. A specific example of a reconfigurable surface with square tiles that can morph between flat, cylindrical (in two different directions), and spherical configurations is presented. One advantage of this method is its convenience in manufacturing. Another merit is its designable (and high) stiffness at all target configurations due to bistability and prestress in the joints. The prestress comes from the bending

deformation of LRBT joints in cylindrical and spherical joints, and thicker substrates introduce larger prestress and correspondingly larger stiffness.

Theoretical aspects of this research are left for future work. Since many bistable elements are employed in a 2D array, a number of bifurcations and intermediate stable states can be created (Puglisi and Truskinovsky, 2000). To design a reliable reconfigurable structure and the corresponding actuation scheme, a theoretical framework that connects the design parameters to the energy landscape of the structure is needed. The framework (similar to the one given in (Li et al., 2019) shall unveil the interaction among kinematic constraints, energy profile of each joint, and the overall energy landscape.

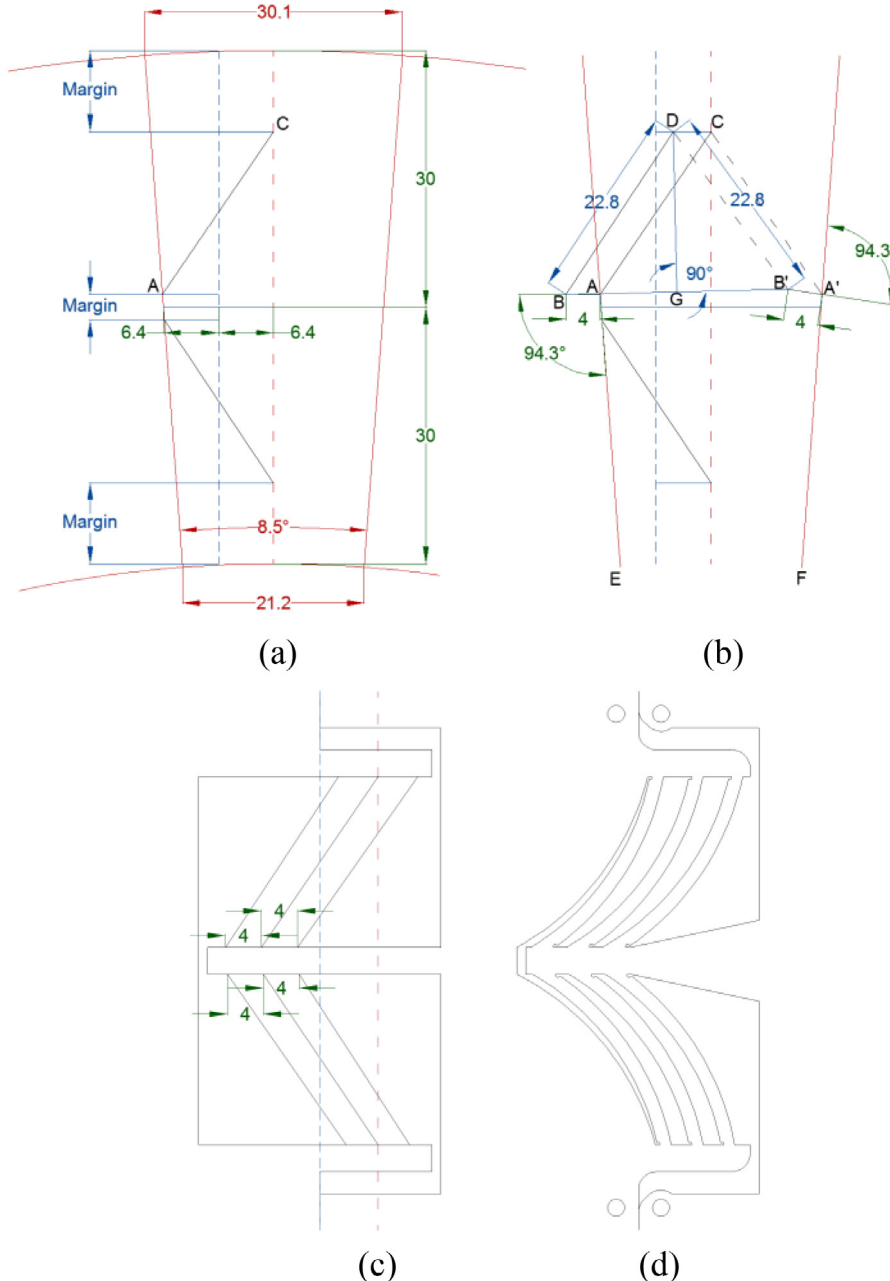


Fig. 27. The drawing procedure of a LTBT joint to match a given large trapezoidal opening and center of rotation.

Further research could also explore the possibility of removing the no-shear condition in Section 2 to achieve more uniform and compact arrangements of tiles, as shown in Fig. 27. Detailed characterization of mechanical properties of the reconfigurable surface would also be of interest.

This concept can be applied to different tile shapes and different target configurations. The general steps are the same with the outline of this paper: (1) identify the compact tile arrangements in 2D where origami-like folding is allowed between tiles to generate isometric transformation; (2) arrange the tiles on a 3D target surface with reasonable adjacency; (3) measure gap types and sizes in between tiles on that 3D surface; (4) design LRBT joints accordingly for all the gaps; (5) assemble LRBT joints and tiles into a continuous 2D structure that can reconfigure to the 3D target shape through metric-changing transformation.

Other features, such as “bistable-rotational” elements (Jeong, 2019), can be integrated. Other applications, such as wearable electronics and robotics, can be explored as well.

Declaration of Competing Interest

The authors declare that they have no known competing financial interests or personal relationships that could have appeared to influence the work reported in this paper.

Acknowledgements

Discussions with David E. (Elliott) Williams, Professor Sergio Pellegrino, and the team of the AFOSR MURI project *Universal Electromagnetic Surface: Exploiting active electronics and active ori-*

gami to generate a programmable electromagnetic response are acknowledged. This paper is based upon work supported by the Air Force Office of Scientific Research under award number FA9550-18-1- 0566 directed by Dr. Ken Goretta.

Appendix A

Design with a specified rectangle opening

As shown in [Section 2](#), a target opening size is given, and the corresponding LRBT joint design needs to be generated. This procedure is demonstrated in this subsection for rectangular openings. Another requirement (other than matching the specified translational opening) is that the center of rotation during bending occurs at the boundary of two connected plates. An example of generating the design shown in [Fig. 5\(a\)](#) is given. The red rectangle in [Fig. 24\(a\)](#) is the target rectangle opening where the red dotted line is the vertical bisector of AD. The blue dotted line is the vertical bisector of AC, and it is the center of rotation during bending. With specified margins due to connecting and mounting requirements (of antenna tiles), the position of beams can be determined. A radius of 30 mm is added to beams reduce the force required to open the hinge. Four holes are for mounting antenna tiles (later). The resultant structure is expected to (1) open to the size of the red rectangle when pulled laterally and (2) to rotate along the blue dotted line when bent.

Design with A Specified Triangle Opening

In this subsection, procedures for generating LRBT joint designs that open into target triangle shapes are provided. In [Fig. 25](#), the red triangle is the target translational opening, and the blue dotted line is the center of rotation during bending. Dimensions of margins (≥ 2 mm) are chosen. A 20° angle between the beam and the blue dotted line is chosen to satisfy Eqs. (13)–(15). The bottom part of the structure connects the two plates with three beams. With the help of contacts, the bottom part equivalently produces a compliant pin-joint connection. Three designs produced according to this drawing procedure ([Fig. 25](#)) are given in [Table 2](#) and [Fig. 12](#). Curvature is not added for $g_t = 20.5$ mm as the beams are slender.

Design with A Specified Trapezoidal Opening

Some target openings take trapezoidal shapes and this subsection introduces a procedure to generate such openings. When the opening is small, the drawing procedure given in [Fig. 26](#) is employed, where the red trapezoid is the target opening. The blue dotted line is the vertical bisector of AB and is the center of rotation during bending.

When the opening is large, where Eqs. (13)–(15) cannot be satisfied using the pattern shown in [Fig. 26](#), the drawing scheme shown in [Fig. 27](#) is employed. Line segment AB has a length of 4 mm and is perpendicular to the blue dotted line. $|AC| = |A'C'|$ defines A'. $|AB| = |A'B'|$ and $\angle BAE = \angle B'A'F$ give B'. DG is the vertical bisector of line segment B'B, which gives point D. As a result, $|BD| = |B'D|$ and BD is the position of an elastic beam. Similarly, the positions of other elastic beams can be worked out, leading to non-symmetric beams.

Appendix B. Supplementary data

Supplementary data to this article can be found online at <https://doi.org/10.1016/j.ijsolstr.2020.09.029>.

References

- Yao, S., Georgakopoulos, S.V., 2018. Origami segmented helical antenna with switchable sense of polarization. *IEEE Access* 6, 4528–4536.
- Wu, Y. et al., 2019. 3D printed modular origami inspired dielectrics for frequency tunable antennas. 2019 IEEE International Symposium on Antennas and Propagation and USNC-URSI Radio Science Meeting.
- Chaudhari, S. et al., 2018. A new class of reconfigurable origami antennas based on E-Textile embroidery. 2018 IEEE International Symposium on Antennas and Propagation & USNC/URSI National Radio Science Meeting.
- Lee, S. et al., 2019. Frequency-reconfigurable antenna inspired by origami flasher. *IEEE Antennas and Wireless Propagation Letters* 18 (8), 1691–1695.
- Khan, M.R. et al., 2019. Origami-enabled frequency reconfigurable dipole antenna. 2019 IEEE International Symposium on Antennas and Propagation and USNC-URSI Radio Science Meeting.
- Fuchi, K. et al., 2012. Origami tunable frequency selective surfaces. *IEEE Antennas and Wireless Propagation Letters* 11, 473–475.
- Fuchi, K. et al., 2017. Frequency tuning through physical reconfiguration of a corrugated origami frequency selective surface. 2017 IEEE International Symposium on Antennas and Propagation & USNC/URSI National Radio Science Meeting.
- Abadi, S.M.A.M.H., Booske, J.H., Behdad, N., 2016. Exploiting mechanical flexure as a means of tuning the responses of large-scale periodic structures. *IEEE Transactions on Antennas and Propagation* 64 (3), 933–943.
- Russo, N.E., Zekios, C.L., Georgakopoulos, S.V., 2019. Origami multimode ring antenna based on characteristic mode analysis. 2019 IEEE International Symposium on Antennas and Propagation and USNC-URSI Radio Science Meeting.
- Liu, X., Yao, S., Georgakopoulos, S.V., 2017. Mode reconfigurable bistable spiral antenna based on kresling origami. 2017 IEEE International Symposium on Antennas and Propagation & USNC/URSI National Radio Science Meeting.
- Georgakopoulos, S.V., 2019. Reconfigurable origami antennas. 2019 International Applied Computational Electromagnetics Society Symposium (ACES).
- Shah, S.I.H., Lim, S., 2019. Thermally beam-direction- and beamwidth-switchable monopole antenna using origami reflectors with smart shape memory polymer hinges. *IEEE Antennas and Wireless Propagation Letters* 18 (8), 1696–1700.
- Carrara, G.P. et al., 2019. A deployable and reconfigurable origami antenna for extended mobile range. 2019 IEEE International Symposium on Antennas and Propagation and USNC-URSI Radio Science Meeting.
- Seiler, S.R. et al., 2018. An origami inspired circularly-polarized folding patch antenna array. 2018 IEEE International Symposium on Antennas and Propagation & USNC/URSI National Radio Science Meeting.
- Zhu, C., Feng, B., 2019. A dual-polarized antenna using an origami structure for 5G emergency communications. 2019 International Workshop on Electromagnetics: Applications and Student Innovation Competition (iWEM).
- Sessions, D.M. et al., 2018. Folding, tessellation, and deployment of an origami-inspired active-material-enabled self-folding reflector antenna. 2018 IEEE International Symposium on Antennas and Propagation & USNC/URSI National Radio Science Meeting.
- Constantine, J. et al., 2016. UHF deployable helical antennas for CubeSats. *IEEE Transactions on Antennas and Propagation* 64 (9), 3752–3759.
- Shah, S.I.H., Tentzeris, M.M., Lim, S., 2019. A deployable quasi-yagi monopole antenna using three origami magic spiral cubes. *IEEE Antennas and Wireless Propagation Letters* 18 (1), 147–151.
- Williams, D.E. et al., 2020. Origami-inspired shape-changing phased array. 50th European Microwave Conference (EuMC). 2020 (to be published). Utrecht, The Netherlands.
- Guy, R.F.E., 1999. Spherical coverage from planar, conformal and volumetric arrays. *IEEE National Conference on Antennas and Propagation*.
- Kildal, P., Martini, E., Maci, S., 2017. Degrees of freedom and maximum directivity of antennas: A bound on maximum directivity of nonsuperreactive antennas. *IEEE Antennas and Propagation Magazine* 59 (4), 16–25.
- Gustafsson, M., Capek, M., 2019. Maximum gain, effective area, and directivity. *IEEE Transactions on Antennas and Propagation* 67 (8), 5282–5293.
- Hawkes, E. et al., 2010. Programmable matter by folding. *Proceedings of the National Academy of Sciences* 107 (28), 12441.
- Paik, J.K., et al. 2011 Robotic Origamis: Self-morphing Modular Robot.
- Peraza-Hernandez, E.A., Hartl, D.J., Malak Jr, R.J., 2013. Design and numerical analysis of an SMA mesh-based self-folding sheet. *Smart Materials and Structures* 22, (9) 094008.
- Gattas, J.M., Wu, W., You, Z., 2013. Miura-base rigid origami: parameterizations of first-level derivative and piecewise geometries. *Journal of Mechanical Design* 135 (11).
- Chen, Y. et al., 2016. Symmetric waterbomb origami. *Proceedings of the Royal Society A: Mathematical, Physical and Engineering Sciences* 472 (2190), 20150846.
- Tachi, T., 2013. Designing freeform origami tessellations by generalizing Resch's patterns. *Journal of Mechanical Design* 135 (11).
- Li, Y., 2020. Motion paths finding for multi-degree-of-freedom mechanisms. *International Journal of Mechanical Sciences* 105709.
- Magliozzi, L. et al., 2017. On the design of origami structures with a continuum of equilibrium shapes. *Composites Part B: Engineering* 115, 144–150.

- Choi, G.P.T., Dudte, L.H., Mahadevan, L., 2019. Programming shape using kirigami tessellations. *Nature Materials* 18 (9), 999–1004.
- Chiang, Y.-C., Mostafavi, S., Bier, H., 2018. Assembly of shells with bi-stable mechanism. In: Proceedings of Advances in Architectural Geometry 2018 (AAG 2018).
- Chen, T., Mueller, J., Shea, K., 2017. Integrated design and simulation of tunable, multi-state structures fabricated monolithically with multi-material 3D printing. *Scientific Reports* 7 (1), 45671.
- Kim, Y. et al., 2018. Printing ferromagnetic domains for untethered fast-transforming soft materials. *Nature* 558 (7709), 274–279.
- Hajiesmaili, E., Clarke, D.R., 2019. Reconfigurable shape-morphing dielectric elastomers using spatially varying electric fields. *10* (1), 183.
- Plucinsky, P. et al., 2018. Patterning nonisometric origami in nematic elastomer sheets. *Soft Matter* 14 (16), 3127–3134.
- Guseinov, R. et al., 2020. Programming temporal morphing of self-actuated shells. *Nature Communications* 11 (1), 237.
- Ma, M. et al., 2013. Bio-inspired polymer composite actuator and generator driven by water gradients. *Science* 339 (6116), 186.
- Page, D.J., 2005. Reconfigurable surface, U.S. Patent, Editor. Jun. 7, 2005: US. p. US 6,903,871 B2.
- Leithinger, D. et al., 2011. Direct and gestural interaction with relief: a 2.5D shape display. In: Proceedings of the 24th Annual ACM Symposium on User Interface Software and Technology. 2011, Association for Computing Machinery, Santa Barbara, CA, USA, pp. 541–548.
- Li, Y., Pellegrino, S., 2019. A theory for the design of multi-stable morphing structures. *Journal of the Mechanics and Physics of Solids* 103772.
- Jacobsen, J.O. et al., 2009. Lamina emergent torsional (LET) joint. *Mechanism and Machine Theory* 44 (11), 2098–2109.
- Wilding, S.E., Howell, L.L., Magleby, S.P., 2012. Introduction of planar compliant joints designed for combined bending and axial loading conditions in lamina emergent mechanisms. *Mechanism and Machine Theory* 56, 1–15.
- Qiu, J., Lang, J.H., Slocum, A.H., 2001. A centrally-clamped parallel-beam bistable MEMS mechanism. In: Technical Digest. MEMS 2001. 14th IEEE International Conference on Micro Electro Mechanical Systems (Cat. No.01CH37090).
- Zhao, J. et al., 2008. Post-buckling and snap-through behavior of inclined slender beams. *Journal of Applied Mechanics* 75 (4).
- Zhang, K. et al., 2017. Origami silicon optoelectronics for hemispherical electronic eye systems. *Nature Communications* 8 (1), 1782.
- Ko, H.C. et al., 2008. A hemispherical electronic eye camera based on compressible silicon optoelectronics. *Nature* 454 (7205), 748–753.
- Huang, Y. et al., 2019. Assembly and applications of 3D conformal electronics on curvilinear surfaces. *Materials Horizons* 6 (4), 642–683.
- Callens, S.J.P., Zadpoor, A.A., 2018. From flat sheets to curved geometries: origami and kirigami approaches. *Materials Today* 21 (3), 241–264.
- Rus, D., Tolley, M.T., 2018. Design, fabrication and control of origami robots. *Nature Reviews Materials* 3 (6), 101–112.
- Zhakypov, Z., Paik, J., 2018. Design methodology for constructing multimaterial origami robots and machines. *IEEE Transactions on Robotics* 34 (1), 151–165.
- Chen, T. et al., 2018. Harnessing bistability for directional propulsion of soft, untethered robots. *Proceedings of the National Academy of Sciences* 115 (22), 5698–5702.
- Abaqus, 2013. Abaqus Documentation Version 6.13. Dassault Systems SIMULIA corp., Providence, RI, USA.
- Leclerc, C. et al., 2017. Characterization of ultra-thin composite triangular rollable and collapsible booms. In: 4th AIAA Spacecraft Structures Conference, American Institute of Aeronautics and Astronautics.
- Ferraro, S., Pellegrino, S., 2018. Self-deployable joints for ultra-light space structures. In: 2018 AIAA Spacecraft Structures Conference, American Institute of Aeronautics and Astronautics.
- Gomm, T., Howell, L.L., Selfridge, R.H., 2002. In-plane linear displacement bistable microrelay. *Journal of Micromechanics and Microengineering* 12 (3), 257–264.
- Delimont, I.L., Magleby, S.P., Howell, L.L., 2015. Evaluating compliant hinge geometries for origami-inspired mechanisms. *Journal of Mechanisms and Robotics* 7 (1).
- Puglisi, G., Truskovsky, L., 2000. Mechanics of a discrete chain with bi-stable elements. *Journal of the Mechanics and Physics of Solids* 48 (1), 1–27.
- Jeong, H.Y. et al., 2019. 3D printing of twisting and rotational bistable structures with tuning elements. *Scientific Reports* 9 (1), 324.